Electrolyte stability determines scaling limits for solid-state 3D Li-ion batteries

Dmitry Ruzmetov[1,2], Vladimir P. Oleshko[3], Paul M. Haney[1], Henri J. Lezec[1], Khim Karki[4], Kamal H. Baloch[4], Amit K. Agrawal[1,2], Albert V. Davydov[3], Sergiy Krylyuk[3], Yang Liu[5], Jian Y. Huang[5], Mihaela Tanase[1,2], John Cumings[4], A. Alec Talin[1]*

[1]Center for Nanoscale Science and Technology
National Institute of Standards and Technology, Gaithersburg, MD 20899

[2]Institute for Research in Electronics and Applied Physics
University of Maryland, College Park, MD 20742

[3]Material Measurement Laboratory
National Institute of Standards and Technology, Gaithersburg, MD 20899

[4]Dept. of Materials Science and Engineering
University of Maryland, College Park, MD 20742

[5]Center for Integrated Nanotechnologies
Sandia National Laboratories, Albuquerque, NM 87123

*E-mail: atalin@nist.gov

RECEIVED DATE (to be automatically inserted after your manuscript is accepted if required according to the journal that you are submitting your paper to)

Rechargeable, all-solid-state Li-ion batteries (LIBs) with high specific capacity and small footprint are highly desirable to power an emerging class of miniature, autonomous microsystems that operate without a hardwire for power or communications. A variety of three-dimensional (3D) LIB architectures that maximize areal energy density have been proposed to address this need. The success of all of these designs depends on an ultra-thin, conformal electrolyte layer to electrically isolate the anode and cathode while allowing Li-ions to pass through. However, we find that a substantial reduction in the electrolyte thickness, into the nanometer regime, can lead to rapid self-discharge of

the battery even when the electrolyte layer is conformal and pinhole-free. We demonstrate this by fabricating individual, solid-state nanowire core-multishell LIBs (NWLIBs) and cycling these inside a transmission electron microscope. For nanobatteries with the thinnest electrolyte, ≈110 nm, we observe rapid self-discharge, along with void formation at the electrode/electrolyte interface, indicating electrical and chemical breakdown. With electrolyte thickness increased to 180 nm the self-discharge rate is reduced substantially and the NWLIBs maintain a potential above 2 V for over 2 h. Analysis of the nanobatteries' electrical characteristics reveals space-charge limited electronic conduction, which effectively shorts the anode and cathode electrodes directly through the electrolyte. Our study illustrates that, at these nanoscale dimensions, the increased electric field can lead to large electronic current in the electrolyte, effectively shorting the battery. The scaling of this phenomenon provides useful guidelines for the future design of 3D LIBs.

Keywords: Lithium ion battery, nanowire, nanobattery, in situ transmission electron microscopy, electrolyte, breakdown, space-charge limited conduction

Rechargeable batteries have become ubiquitous in modern society, powering a host of seemingly indispensable portable electronics and communications devices [1]. Combined with energy scavenging mechanisms, rechargeable batteries are also desirable for energizing autonomous micro-electro-mechanical systems (A-MEMS) that operate remotely without a hardwire for either power or communications [2], and which are increasingly used in biology [3], medicine [4], environmental monitoring [5], agriculture [6], and intelligence gathering. Due to their high energy density, Li-ion batteries (LIBs)

are attractive for these applications, and all-solid-state LIBs add many further benefits, including compatibility with MEMS manufacturing, relatively long lifetimes, generally negligible self-discharge rates, and enhanced safety owing to the lack of flammable and/or toxic liquid-phase electrolytes. However, the low areal energy densities of commercial thin film LIBs (TFLIBs) combined with typical energy demands limits the miniaturization of most prototype A-MEMS to the millimeter range. In fact, the size of the battery often exceeds the dimensions of the rest of the device by several orders of magnitude [7]. TFLIBs as small as 50 μm x 50 μm have been demonstrated [8] using the approach pioneered by Bates et al. [9], using physical vapor deposition of three active layers: a $LiCoO_2$ cathode, a nitrogen-doped Li_3PO_4 solid electrolyte (LiPON), and Li anode. These TFLIBs retain over 90 percent of their initial energy capacity after 40,000 cycles and are now commercially available [10]. However, with typical energy capacity per unit area of 0.01 J/mm^2 to 0.03 J/mm^2, these batteries store insufficient energy for most potential applications envisioned for A-MEMS, even when combined with a photovoltaic or vibrational energy harvesting device [2]. Increasing the thickness of the battery electrodes to store more energy reduces power capability, because ions must diffuse longer distances. Ultimately, the fracture toughness of the active layers places an upper limit on the electrode thickness, because the stress induced by Li intercalation scales with the electrode thickness. For $LiCoO_2$, one of the most widely employed cathode materials, this limit is a mere 4 μm [1], limiting the capacity far below the targets for many emerging applications.

The answer to the energy challenge is to amplify the areal energy density while maintaining fast kinetics. A number of three dimensional (3D) LIB designs based on

trenches, inverse opals, vertical rods, and periodic 'sponges' have been proposed [11, 12], but a complete, fully-3D LIB has yet to be experimentally demonstrated. Regardless of the specific 3D geometry, reducing electrode feature dimensions and the inter-electrode separation improves power performance by minimizing electron and ion diffusion times and by limiting Ohmic losses. Reductions in feature sizes also increase the interface area, lowering the local current density and the associated charge transfer overpotentials. Unfortunately, the increased interface area also requires more solid electrolyte, which functions as the electrode separator but does not itself carry any energy storage capacity. In commercial TFLIBs the LiPON electrolyte is typically 1 μm to 2 μm thick [10], and using similar LiPON thickness in a 3D architecture would require electrode features of about 10 μm to maintain the electrolyte volume fraction at 10% or less. Such dimensions would again raise concerns about fracture and sluggish charge-transport kinetics. Substantially reducing the solid electrolyte thickness to below 1 μm is therefore essential for further increasing the power and energy density of 3D LIBs. At first glance, this would simply entail the successful deposition of a uniform, pinhole-free electrolyte layer over a potentially complex surface incorporating high-aspect-ratio structures. However, as we show in this Letter, at thickness substantially smaller than 1 μm, the ability of the electrolyte to prevent electronic current flow between the anode and cathode and its chemical stability may be drastically compromised due to the onset of space charge limited conduction.

To understand how LIBs behave at reduced dimensions, we fabricate complete nanobatteries using Si nanowires as a template onto which the various battery components are sequentially deposited using physical vapor deposition, resulting in a

core-multishell geometry (see Fig. 1 and the methods section for details). Each nanowire LIB (NWLIB) consists, from center to exterior, of a Si nanowire metalized with Ti/Pt/Ti and coated with $LiCoO_2$ (cathode), followed by LiPON solid electrolyte, and an n-doped amorphous Si anode. The layers are deposited subsequently, with a 700 ^oC annealing in oxygen step following the $LiCoO_2$ deposition. At 0.5 μm to 1 μm in diameter and up to 7 μm in length, the NWLIBs are the smallest, complete secondary batteries realized to date.

We use three distinct approaches to characterize individual NWLIBs. The first two approaches use focused ion beam (FIB) milling and electron beam induced deposition (EBID) to locate, prepare, and contact individual NWLIBs, as shown in Fig. 1f. The first approach utilized a highly insulating support of a 600 nm thermal SiO_2 layer atop a Si substrate, and the second approach used a free-standing 50 nm thick SiN_x support, allowing for simultaneous *in-situ* transmission electron microscopy observations. In the third approach, we use a tungsten tip controlled by a nanomanipulator to contact individual NWLIBs directly on the fabrication substrate inside of a transmission electron microscope (TEM). In the first two approaches, we deposited the NWLIB onto the support from isopropanol suspension and then use FIB milling to expose the Ti/Pt/Ti cathode current collector near the narrow end of the NWLIB. This is followed by EBID of Pt to connect the anode and cathode to nearby lithographically-defined metal pads. For each NWLIB, near the cathode contact, a 'ring' of the amorphous Si anode is removed by FIB to electrically isolate the anode and cathode. In addition to NWLIBs, thin film LIBs (TFLIBs) are fabricated as experimental control specimens using the same procedure starting with flat Si/SiO_2 substrates. A bright-field TEM cross sectional image for an uncycled TFLIB is shown in Fig. S1b, in the supplementary information (SI).

By focusing on individual nanobatteries, we eliminate the effects of collective behavior characteristic of large arrays, which simplifies interpretation of results and reduces the probability that a fabrication defect leads to catastrophic failure. Most importantly, the small dimensions allow us to image the entire NWLIB in a TEM, or scanning TEM (STEM) and observe changes in the microstructure during electrochemical cycling. Previously, nanoscale LIBs have been assembled inside TEMs for the purpose of *in situ* structural characterization during cycling [13]. However, those one-of-a-kind nanobatteries could not be integrated into a microsystem, nor were their current-voltage-time characteristics reported. Alternatively, thin cross sections of all-solid-state thin film batteries have been imaged in the TEM [14, 15]. While extremely informative, thin film cross sections are difficult to handle, are much more sensitive to FIB damage, and do not capture the radial geometry characteristic of most proposed 3D LIB designs. Our NWLIBs constitute a flexible integrated platform for *in situ* electrochemical experiments compatible with TEM, STEM, and FESEM aimed at imaging and analyses of the microstructural changes that accompany charge transfer and correlating these with the observed electrical characteristics. Our scheme results in the fabrication of a large number, $\approx 10^6/cm^2$, of nearly identical specimens. Furthermore, each NWLIB is stable in air prior to charging, facilitating transport and measurement using different instruments and techniques.

Constant current charging-open circuit potential (CCC-OCP) curves for a NWLIB with a ≈110 nm thick LiPON and supported by highly insulating SiO_2 are shown in Fig. 2a. Two slow scan linear voltammetry (I-V) sweeps collected just prior to CCC-OCP measurement are shown in Fig. 2b. CCC-OCP and I-V sweeps for a NWLIB with 180 nm

thick LiPON are shown in Figs. 2c and 2d, respectively. During charging, the voltage for both NWLIBs initially rises to >5 V, then decreases before stabilizing at ≈4 V. Once the charging current is turned off, the OCP for the thinner LiPON NWLIB drops rapidly to <0.5 V. For the NWLIB with 180 nm LiPON, the OCP initially drops to ≈2.3 V and remains above 2 V for over 2 h. Several other NWLIBs with the thinner LiPON and one other NWLIB with the thicker LiPON were also tested and showed similar behavior. For comparison, CCC-OCP-constant current discharge and I-V sweeps collected for a TFLIB (LiPON thickness ≈320 nm) are shown in Fig. 2e and 2f, respectively. As with NWLIBs, during charging the potential initially rises sharply (≈7 V), then decreases before rising again. The exact origin of this peak is presently unknown, but a similar peak was observed by Baggetto *et al.* during initial charging of a Si electrode coated with LiPON and immersed in an organic electrolyte with a Li metal counter electrode. The authors attributed the effect to an interfacial layer forming at the Si/LiPON interface during deposition [16]. We observed no such interfacial layer, suggesting that the voltage spike may be inherent to Li transport across the Si/LiPON interface. Unlike the NWLIBs, the TFLIB does not rapidly self- discharge, and can instead be intentionally discharged at constant current with a stable capacity of ≈16 μA-h/cm^2 for more than 10 cycles, as shown in Fig. S2 in supplementary information. TFLIBs with LiPON layer thickness ≈100 nm were also fabricated, but appeared electrically shorted, possibly due to pinholes, a hazard of the TFLIB geometry. No such pinhole shorting is observed for the NWLIBs chosen for electrical characterization. A short like this would likely cause Ohmic I-V characteristics, which is contrary to our observation that both NWLIBs display resistance >2 TΩ at 1 V.

TEM images of the NWLIBs show a high quality dense LiPON layer with no readily observed defects, but despite this, both thicknesses of LiPON fabricated show significant self-discharging. The NWLIBs with the thinnest LiPON rapidly and completely self-discharge, and those with thicker LiPON maintain OCP >2V for only ≈2 h, indicating that electronic transport is still taking place across the thin LiPON electrolyte. To better understand the origin of the electronic current, we next examine in detail the NWLIB I-V characteristics. I-V sweeps for the NWLIBs exhibit the following three distinctive features: 1) the current increases sharply at a threshold voltage that depends on LiPON thickness; 2) there is hysteresis, such that the effective resistance is higher on the upward voltage sweep than on the downward voltage sweep; 3) the current scales as a power law with voltage, $I \propto V^n$, with n≈1 at low V during the upward sweep, and n≈2 at higher V and during the downward voltage sweep, as shown in Fig. 3 where the log I vs. V is plotted for the NWLIB with 110 nm thick LiPON. Similar characteristics have been observed in other devices, namely thin insulating films of various transition metal oxides and perovskites, sandwiched between two conductor electrodes [17]. As discussed in previous works and as we show here, the theory of trap-controlled space charge limited conduction (SCLC) can explain these features [18].

Transport characteristics are governed by SCLC when the injected charge density exceeds the equilibrium thermal charge density n_o [18]. At low charge injection, electron transport is Ohmic: $J = e\mu n V/d$, where e, μ, and n are the electron charge, mobility, and density, respectively, V is the applied voltage, and d is the insulator thickness. The current-voltage relation in the SCLC regime is given by $J = \frac{9}{8}\varepsilon\mu\frac{V^2}{d^3}$, where ε is the dielectric constant of the insulator. In the trap-free case, the transition from Ohmic to

SCLC occurs at a cross over voltage $V^* = \frac{8}{9}\frac{en}{\varepsilon}d^2$. The dependence of *V** on the insulator thickness squared has important implications for nanobatteries as we discuss below. The effect of traps, or localized energy levels found in most insulators, is to change the crossover from Ohmic to SCLC regimes in a manner that depends on the details of the traps' energy distribution. We assume a distribution of trap energies given as $D(E) = \frac{N_t}{kT_c}\exp[(E - E_c)/kT]$, where T_c parameterizes the trap distribution in energy and N_t is the trap density. Finally, we suppose that the escape rate of trapped charge is small compared to the voltage scan rate, so that the occupation of a trap state persists throughout an I-V scan.

Following the analysis of Lampert and Mark [18], we obtain three distinct regimes in the I-V characteristics. At low voltage, and therefore low charge injection, the transport is approximately Ohmic, $J \propto V$. There is a transition at the voltage (see also SI) $V_1^* = V_o\frac{\Gamma(l+1)^2}{l(2l+1)}$, where $V_o = \frac{en_o\mu d}{\varepsilon}$, $\Gamma = \left(\frac{N_t}{n_o}\right)\left(\frac{n_o}{N_c}\right)^{1/l}$, $l=T_c/T$, and N_c is the effective density of states for charge carriers. For voltages above V_1^*, progressively more traps are filled so that an increasing fraction of injected charge contributes to transport. Just above V_1^*, $J \propto V^{(l+1)}$ and the current increases rapidly. The second transition occurs at $V_2^* = \frac{4}{3}V_o\left(\frac{\Gamma(l+1)^2}{l(2l+1)}\right)^{l/l-1}$. Above this voltage, the traps are filled so that all injected charges participate in transport, and here the trap-free, ideal SCLC behavior is recovered, with $J \propto V^2$. For the downward voltage scan, we assume all the traps are filled, and we take the current to be the sum of thermal and SCLC contributions. Fig. 3 shows excellent agreement between experimental and calculated I-V characteristics for the NWLIB with the thin (d=110 nm) LiPON electrolyte.

Trap-controlled SCLC can discharge a battery either via electron de-trapping, or from direct electron transport from anode to cathode and concomitant Li transport in the same direction. To determine the relative importance of these processes, we first consider electron de-trapping. Based on the model fit to the experimental data, the trap density is estimated to be $N_t \approx 10^{17}$ cm^{-3}, which, given the NWLIB dimensions, yields a total charge of $\approx 10^{-13}$ C. However, charge/discharge curves indicate that appreciable discharge requires $\approx 10^{-9}$ C. Moreover since the total number of traps scales with layer thickness, batteries with thicker LiPON would be more susceptible to discharge, contrary to observations. It is therefore more likely that direct electron transport is responsible for the observed I-V characteristics and also for the battery self-discharge. In this case, the electrolyte thickness is crucial, since the onset of large currents (V_1^*) scales as d^2 [18]??. The insulator thickness also appears in the SCLC pre-factor, $J \propto d^{-3}$, which indicates a steep dependence of the leakage current on thickness.

SCLC theory neglects the role of the contact-insulator interface. For aqueous electrolytes, this interface is all-important, due in part to the extremely short Debye length of the electrolyte (which implies that the potential drop is localized at the interface). However in solid-state electrolytes, the potential drop has been observed to extend far into the electrolyte layer [15], so that the picture of bulk-limited SCLC is applicable.

SCLC is fundamentally a bulk-limited transport mechanism, implying facile injection of charge at the contacts ($LiCoO_2$ and Si, in the present case). Indeed, Yu *et al.* reported large electronic current for a 1.5 μm thick LiPON layer sandwiched between Pt electrodes (a Li-ion blocking metal) at a potential of ≈5.5 V, together with the formation

of bubbles at the positive electrode [19]. They also reported a pronounced change in the impedance characteristics suggesting formation of an interfacial layer with large capacitance. To explain the bubble formation and the apparent breakdown of LiPON, these workers proposed the following chemical reaction involving the breaking of P-O bonds, formation of P-O-P chains, and releasing free oxygen:

$$2Li_3PO_4 \rightarrow Li_4P_2O_7 + \frac{1}{2}O_2 + 2Li^+ + 2e^- \qquad (1)$$

To determine whether breakdown of LiPON was occurring in our case, we performed electrochemical cycling of a NWLIB mounted on a Si chip with a 50 nm thick SiN_x membrane window and patterned Au electrodes inside a TEM. A series of TEM images is collected prior to charging to ensure that the microstructure is stable and that the electron beam is not appreciably damaging the LiPON layer. The NWLIB is then biased from 0 V to 4.2 V in 0.01 V increments over 20 min period, at which point another series of TEM images is collected (the electron beam is blanked off during the charging). The NWLIB is then cycled 7 times between 2.5 V (discharged state) and 4.2 V (charged state) over a period of nine hours, and the final images is collected. The net current flowing through the battery cannot not be determined precisely because the Si chips with nitride membranes and large-area contacts exhibit current leakage with a voltage dependent resistance similar to that of the NWLIBs, as shown in Fig. S3 in supplementary information. Images collected initially, after first charge, and after repeated cycling are shown in Fig. 4a, 4b, and 4c, respectively. As seen in the TEM images, after the NWLIB is biased to 4.2 V, a striped pattern appears in LiPON and a brighter contrast can be observed along the $LiCoO_2$/LiPON boundary (Fig. 4b). The bright areas can be interpreted as voids and expanded substantially following seven

charge discharge cycles (Fig. 4c). Following the *in situ* TEM characterization, the NWLIB is examined *ex situ* in a field-emission STEM (and TEM) operating at 300 kV, which allows higher resolution and contrast images to be collected. High-angle annular dark field (HAADF) STEM examination of the same NWLIB confirmed the appearance of voids, as indicated by yellow arrows in Figs. 4d and 4e. For comparison, another NWLIB that was not cycled and was lying nearby on the SiN_x grid is also imaged and does not show presence of voids (Fig. 4f), under similar imaging conditions. Using lowest intensities and blanking of electron beams to minimize radiation damage, we do not observe formation of the voids in both cycled and pristine NWLIBs after several hours of examination under the chosen conditions.

To further explore the nanosctructural changes in the batteries upon cycling and to confirm that the observed bubble formation in the LiPON electrolyte is due to cycling and not due to electron damage in the TEM, a NWLIB was electrically tested directly on the fabrication substrate through our third characterization method in a TEM holder equipped with a piezomanipulator that has been described previously [13, 20]. Figure 5a shows a pristine NWLIB directly grown on the substrate after contacting with a tungsten tip. The substrate and the tungsten tip served as current collectors in the electrochemical cycling. During charging or discharging, a positive or negative potential was applied to the substrate with respect to the tungsten tip, respectively. During the first charging, the voltage applied to the substrate was gradually increased up to 50 V, and a current in the order of several nA was detected. This large voltage is characteristic of the highly insulating tungsten oxide contact, which helps to limit the current in these tests. During the first charging, a void was formed at the $LiCoO_2$/LiPON interface, as pointed by the

yellow arrow in Figure 5b. Interestingly, the void healed after discharge at a bias of -40 V (Fig. 5c). During the second charging/discharging cycle, the void at the $LiCoO_2$/LiPON interface appeared/disappeared again, as shown in Figure 5d and 5e. Figure 5f and 5g are higher magnification views of the areas marked by blue and red dotted rectangles in Figure 5d and 5e, respectively, showing clearly a void was formed at the $LiCoO_2$/LiPON interface after charging and disappeared after discharging.

We have explored the possibility that the reaction described by Eq. (1) induces discharge via release and subsequent extraction of charge carriers (either Li^+ ions or electrons). This possibility is ruled out by noting that the number of charges collected during a single I-V scan exceeds the total number of atoms in the electrolyte. Moreover, the number of charges collected exceeds the Li capacity of the electrodes, so that the only scenario physically consistent with the data is electron injection and collection.

In summary, substantial reduction in the electrolyte thickness below 100 nm can lead to rapid self-discharge of the battery even when the electrolyte layer is conformal and pinhole-free as demonstrated by *in situ* cycling of individual, solid-state heterostructure NWLIBs. This problem may be addressed by using a different electrode/electrolyte combination or by inserting a thin Li-ion-transparent layer between the electrode(s) and LiPON to prevent electron/hole injection. Illustrating the importance of electric fields in the electrolyte, this work provides useful guidelines for optimal design of long-cycling life miniaturized 3D LIBs.

Methods

Fabrication of NWLIBs and TFLIBs. Fabrication of NWLIBs starts with Si nanowires (≈170 nm in diameter) grown by Au-catalyzed VLS on Si (111) substrates according to a previously reported recipe [21]. After removal of the Au catalyst nanoparticles using a

Au etch solution, the nanowires are coated with ≈10 nm Ti, followed by ≈30 nm Pt, ≈40 nm Ti, and ≈180 nm of $LiCoO_2$, all using sputter deposition in the same chamber and without exposure to air (see SI for more details). We estimate the uncertainty in the thickness of individual layers to be ≈15 % based on comparison of measurement made with cross section SEM, TEM and mechanical profilometry (used only for TFLIBs). The coated nanowires are then annealed in ambient oxygen at 700 ^{o}C for 2 h. Following the heat treatment, the samples are sputter-coated with ≈110 nm of LiPON or ≈180 nm of LiPON, and finally ≈35 nm of phosphorus-doped amorphous Si. FESEM images of NWLIBs collected at different stages of fabrication are shown in Figs 1a-d, along with a fractured cross section (Fig. 1d) and a 3D schematic of a NWLIB (Fig. 1e), respectively. Our fabrication scheme results in simultaneous production of a large number (> $10^6/cm^2$) of NWLIBs (Fig. 1h). Thin-film LIBs (TFLIBs) are fabricated alongside the NWLIBs starting with Si wafers coated with 100 nm of thermal oxide. The $LiCoO_2$, LiPON, a-Si layer thicknesses for the TFLIBs are ≈400 nm, ≈360 nm, and ≈80 nm, respectively, with the difference in thickness due to the different substrate geometry. X-ray diffraction (XRD) and electron backscatter diffraction (EBSD) patterns collected after fabrication confirm that the $LiCoO_2$ crystallizes in the hexagonal phase (R-3m space group) with a preferred (00.3) orientation nearly perpendicular to the Si nanowire [111] axis (see Fig. S4 and S5). Pt dots with diameters of 940 μm are defined on the top TFLIB a-Si layer and served as the anode current collectors.

Following deposition, NWLIBs are suspended in isopropanol using sonication and then drop-cast onto Si wafers with 600 nm of thermal oxide and Pt contact pads deposited evaporation through a shadow mask. A dual beam FIB is used to expose the

inner Ti/Pt/Ti cathode current collector and electrically isolate the anode from the cathode by removing a 'ring' of Si. Electron beam induced deposition is then used to connect the anode and cathode electrodes to the Pt contact pads. Integrated NWLIB on a 600 nm thick SiO_2/Si and on a 50 nm SiN_x membrane are shown in Figs. 1f and 1g, respectively.

In situ and ex situ electrical testing/electron microscopy and characterization. Slow scan linear sweep voltammetry (I-V), constant current charge-open circuit potential-constant current discharge (I-t) characteristics for the NWLIBs and the TFLIBs are collected using a computer controlled current/voltage source/measure unit with an input impedance of $>10^{14}$ Ω and 10 fA resolution according to the manufacturer, as well as a commercial potentiostat (used only for the thin film batteries). The NWLIB electrochemical measurements are performed either in a FESEM retrofitted with two electrical nanomanipulators or in a LaB_6 JEOL TEM 2100 and in an FEI Tecnai F 30 TEMs with custom specimen stages designed for *in situ* electrical measurements. The TFLIBs are electrically characterized in an Ar-filled glove box. As-fabricated NWLIBs also are analyzed using a FESEM equipped with an electron backscatter diffraction (EBSD) detector. Medium and high-resolution S/TEM imaging of pristine and cycled NWLIBs and TFLIBs are performed in a field-emission FEI Titan 80-300 analytical S/TEMs operating at 300 kV accelerating voltage. X-ray diffraction (XRD) scans are collected on a scanning microdiffractometer equipped with a general area detector diffraction system using Cu Kα radiation.

Certain commercial equipment, instruments, or materials are identified in this document. Such identification does not imply recommendation or endorsement by the National Institute of Standards and Technology, nor does it imply that the products identified are necessarily the best available for the purpose.

Acknowledgement

Dmitry Ruzmetov acknowledges support under the Cooperative Research Agreement between the University of Maryland and the National Institute of Standards and Technology Center for Nanoscale Science and Technology, Award 70NANB10H193, through the University of Maryland. Vladimir Oleshko acknowledges support by National Institute of Standards and Technology (Contracts SB134110SE0579 and SB134111SE0814).

Figures

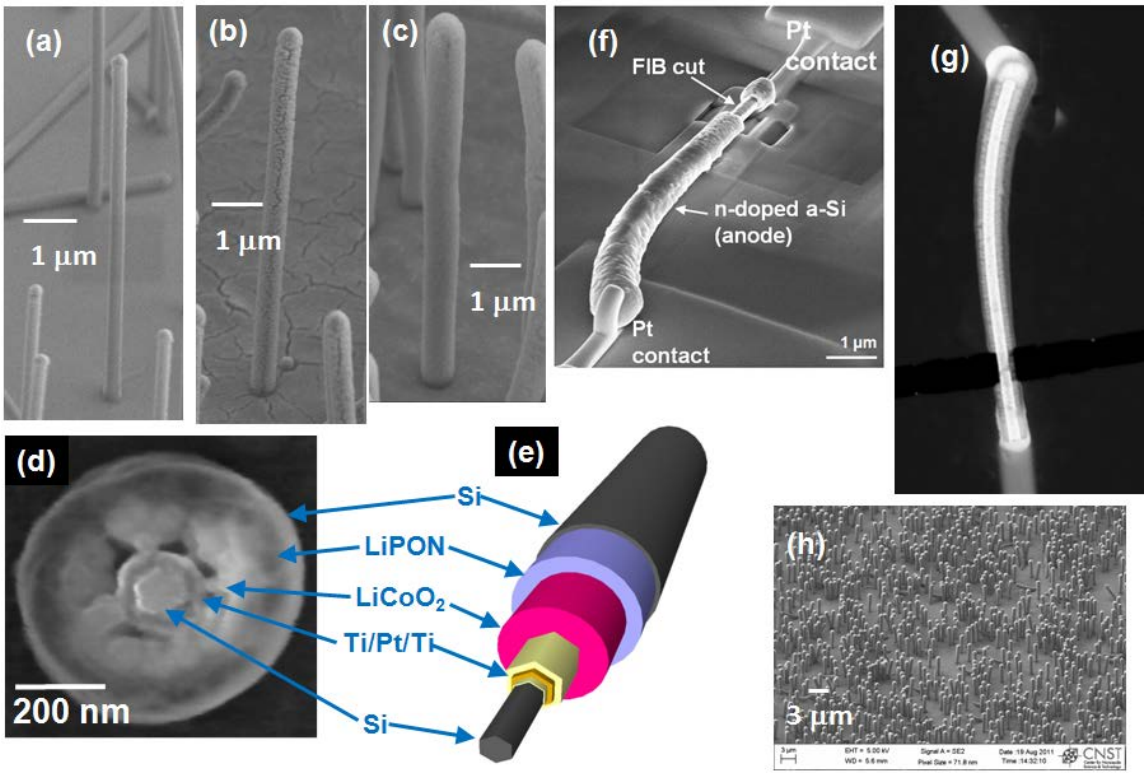

Figure 1. FESEM (a,b, c) images of NWLIBs following deposition of (a) Ti/Pt/Ti, (b) $LiCoO_2$, and (c) LiPON/Si, (d) a FIB cut cross section FESEM image and (e) a NWLIB schematic, (f) a NWLIB contacted with Pt electrodes on a Si/SiO_2 substrate, (g) HAADF STEM of a NWLIB on SiN_x membrane with Pt contacts showing its internal structural arrangement, (h) a panoramic FESEM of the NWLIBs on the wafer.

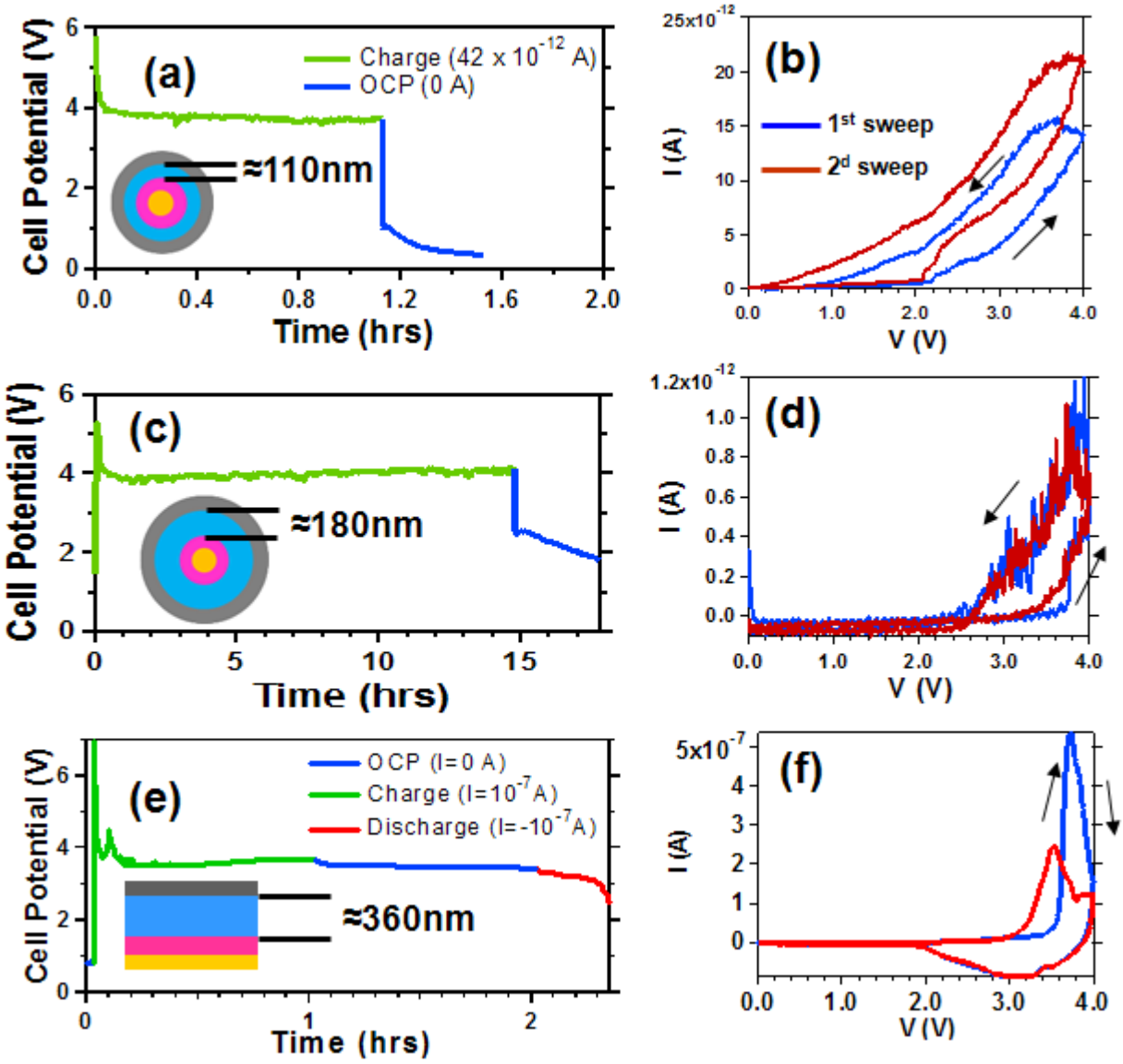

Figure 2. Constant current charge-open circuit potential characteristics (a) and slow scan I-V characteristics (b) NWLIB with 110 nm thick LiPON; (c), (d) NWLIB with 180 nm thick LiPON; (e), (f) a thin film LIB with 360 nm thick LiPON (discharge shown in red). The voltage scan rate for I-V curves is 0.16 mV/s.

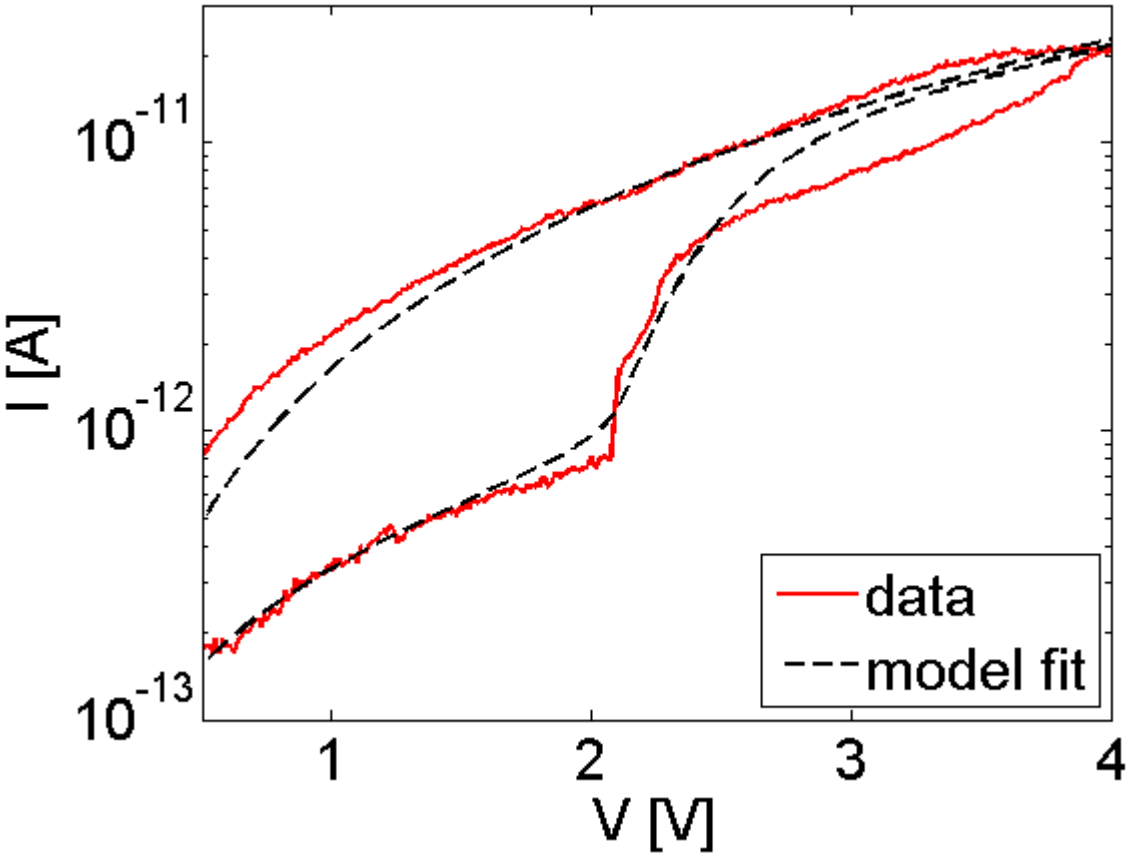

Figure 3. Measured and calculated I-V characteristics for the NWLIB with LiPON≈110 nm (same data as in Fig. 2b). Model parameters are: $N_c = 2\times10^{19}\,\mathrm{cm}^{-3}$, $n_0 = 3.5\times10^{16}\,\mathrm{cm}^{-3}$, $\mu = 4.5\times10^{-9}\,\mathrm{cm}^2/\mathrm{V\cdot s}$, $N_t = 10^{18}\,\mathrm{cm}^{-3}$, $\epsilon = 32$, $\ell = 10$.

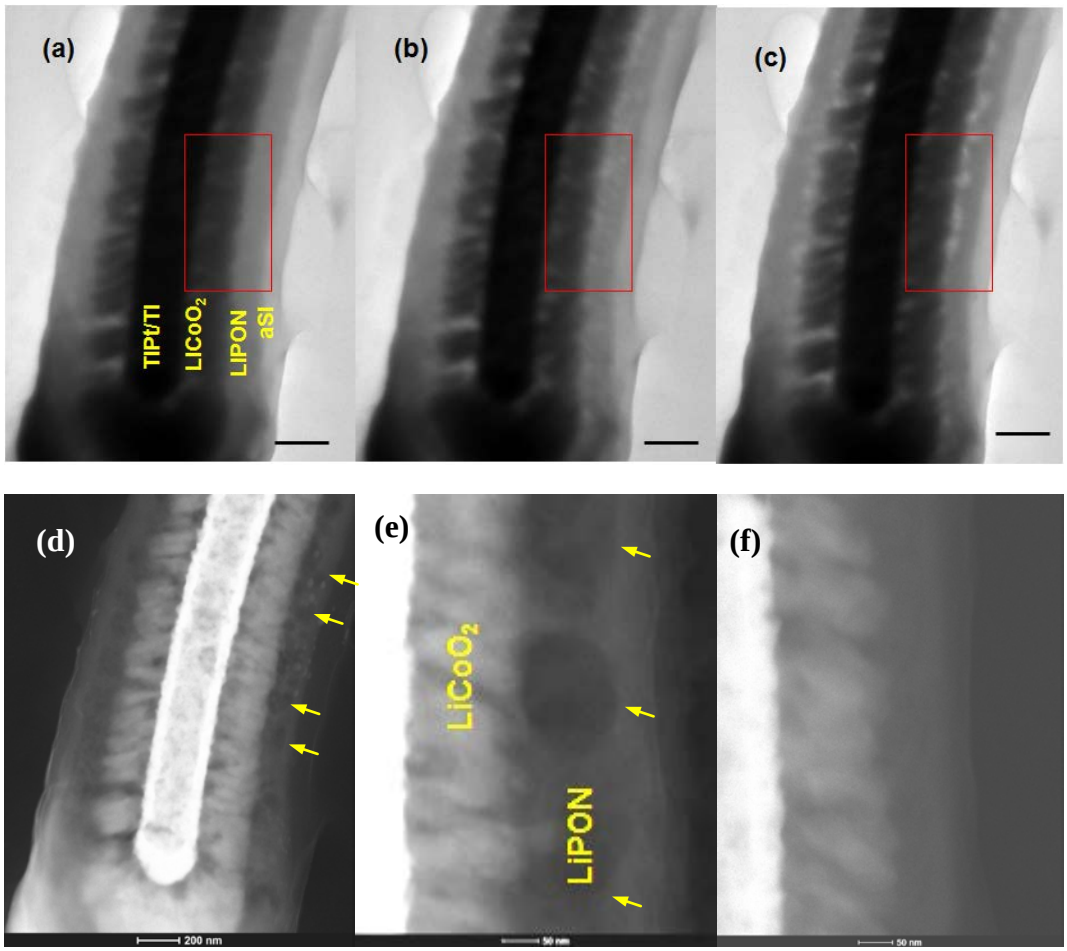

Figure 4. *In situ* TEM testing of a NWLIB. (a) Before charging (red box includes $LiCoO_2$/LiPON interface) (b) after 1st discharge, LiPON in the box has a striped texture. (c) After 7th charge/discharge cycles voids appear at LiPON/$LiCoO_2$ interface. The scale bar corresponds to 200 nm. (d, e) *Ex situ* HAADF STEM of the same NWLIB after cycling, 50 nm to 100 nm voids appear at or near the LiPON/$LiCoO_2$ interface as indicated by the yellow arrows. (f) An enlarged area of an uncycled NWLIB from the same batch included for comparison with image (e).

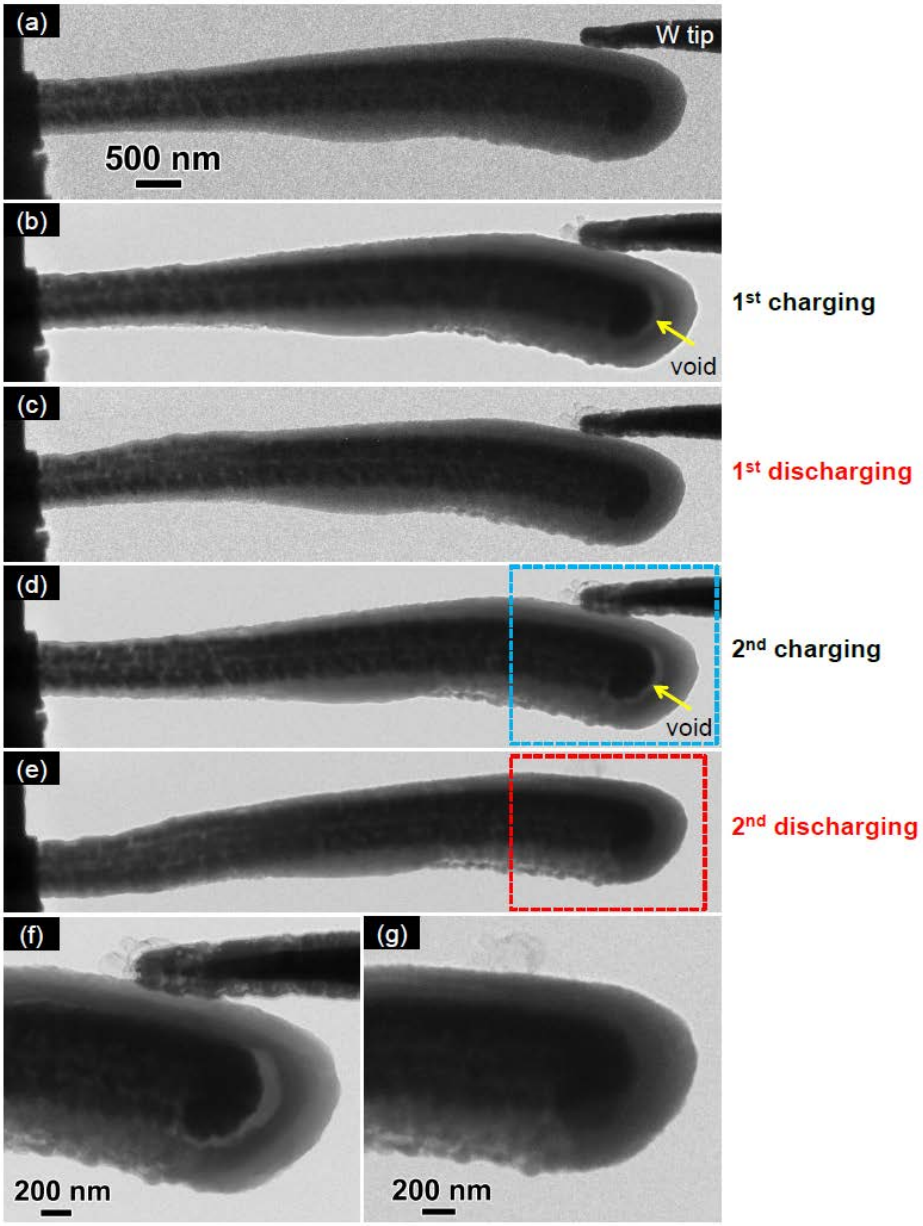

Figure 5. Microstructure evolution of a NWLIB during cycling inside a TEM. (a) A pristine NWLIB directly grown on a Si substrate was contacted by a tungsten tip. During cycling, the potential is applied to the substrate with respect to the tungsten tip, and the substrate as well as tungsten tip served as current collectors. (b) After the first charging, a void is formed at the $LiCoO_2$/LiPON interface, as indicated by the yellow arrow. (c) The void is healed after discharge. (d-e) The second charge/discharge cycle showing the formation and disappearance of the void at the $LiCoO_2$/LiPON interface. Note that the tungsten tip was extracted away after the second discharge. (f) Higher magnification view of the area marked by blue dotted rectangle in (d), showing a void is formed at the $LiCoO_2$/LiPON interface. (g) Higher magnification view of the area marked by red dotted rectangle in (e), showing the void is healed again after discharge.

References

[1] M. Armand and J. -M. Tarascon, *Nature,* vol. 451, p. 652, 2008.

[2] F. Albano, Y. S. Lin, D. Blaauw, D. M. Sylvester, K. D. Wise and A. M. Sastry, *J. Power Sources,* vol. 185, p. 1524, 2008.

[3] A. J. Nieder, *Neurosci. Methods,* vol. 101, p. 157, 2000.

[4] E. A. Johannessen, L. Wang, C. Wyse, D. R. S. Cumming and J. M. Cooper, *IEEE Trans. Biomed. Eng.,* vol. 53, p. 2333, 2006.

[5] M. Hautefeuille, C. O'Mahony, B. O'Flynn, K. Khalfi and F. Peters, *Microelectron. Reliab.,* vol. 48, p. 906, 2008.

[6] L. Ruiz-Garcia, L. Lunadei, P. Barreiro and J. I. Robla, *Sensors,* vol. 9, p. 4728, 2009.

[7] T. S. Arthur, D. J. Bates, N. Cirigliano, D. C. Johnson, P. Malati, J. M. Mosby, E. Perre, M. T. Rawls, A. L. Prieto and B. Dunn, *MRS Bulletin,* vol. 36, p. 523, 2011.

[8] W. C. West, J. F. Whitacre, V. White and R. B. V., *J. Micromech. Microeng.,* vol. 12, p. 58, 2002.

[9] J. B. Bates, N. J. Dudney, B. Neudecker, A. Ueda and C. D. Evans, *Solid State Ionics,* vol. 135, p. 33, 2000.

[10] See for example http://www.excellatron.com/advantage.htm or http://www.st.com/internet/analog/product/250531.jsp.

[11] J. W. Long, B. Dunn, D. R. Rolison and H. S. White, *Chem. Rev.,* vol. 104, p. 4463, 2004.

[12] M. Nathan, D. Golodnitsky, V. Yufit, E. Strauss, T. Ripenbein, I. Shechtman, S. Menkin and E. Peled, *JOURNAL OF MICROELECTROMECHANICAL SYSTEMS* , vol. 14, p. 879, 2005.

[13] J. Huang, L. Zhong, C. M. Wang, J. P. Sullivan, W. Xu, L. Q. Zhang, S. X. Mao, N. S. Hudak, X. H. Liu, A. Subramanian, H. Y. Fan, L. Qi, A. Kushima and J. Li, *Science,* vol. 330, p. 1515, 2010.

[14] A. Brazier, L. Dupont, L. Dantras-Laffont, N. Kuwata, J. Kawamura and J. M.

Tarascon, *CHEMISTRY OF MATERIALS* , vol. 20, p. 2352, 2008.

[15] K. Yamamoto, Y. Iriyama, T. Asaka, T. Hirayama, H. Fujita, C. A. J. Fisher, K. Nonaka, Y. Sugita and Z. Ogumi, *ANGEWANDTE CHEMIE,* vol. 49, p. 4414, 2010.

[16] L. Baggetto, R. A. H. Niessen and P. H. L. Notten, *ELECTROCHIMICA ACTA* , vol. 54, p. 5937, 2009.

[17] S. Kim, H. Y. Jeong, S. -Y. Choi and Y. -K. Choi, *Appl. Phys. Lett.,* vol. 97, p. 033508, 2010.

[18] M. A. Lampert and P. Mark, Current Injection in Solids, New York: Academic Press, 1970.

[19] X. Yu, J. B. Bates, G. E. Jellison and F. X. Hart, *J. Electrochem. Soc.,* vol. 144, p. 524, 1997.

[20] X. H. Liu and J. Y. Huang, *Energy Environ. Sci.*, vol. 4, p. 3844, 2011.

[21] S. Krylyuk, A. V. Davydov and I. Levin, *ACS Nano,* vol. 5, p. 656, 2011.

Supplementary Information

Electrolyte stability determines scaling limits for solid-state 3D Li-ion batteries

Dmitry Ruzmetov, Vladimir P. Oleshko, Paul M. Haney, Henri J. Lezec, Khim Karki, Kamal H. Baloch, Amit K. Agrawal, Albert V. Davydov, Sergiy Krylyuk, Yang Liu, Jian Y. Huang, Mihaela Tanase, John Cumings, A. Alec Talin.

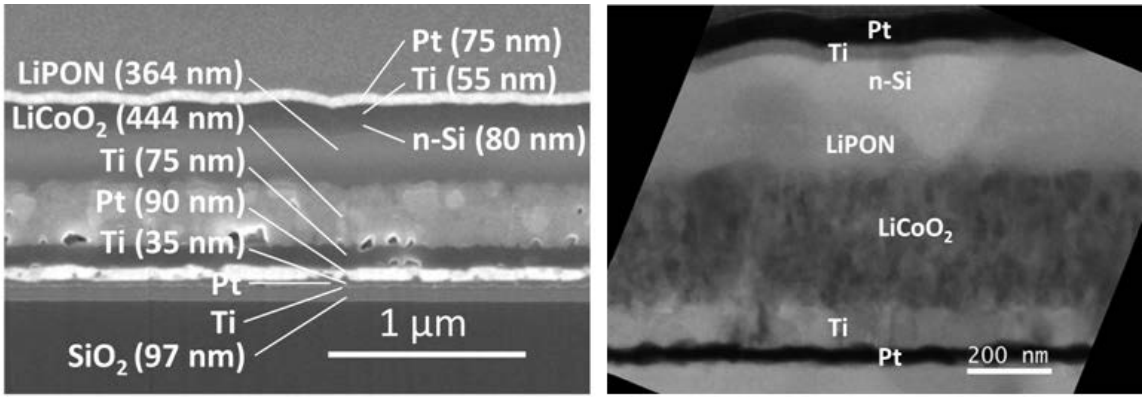

Fig. S1(a) FESEM and (b) TEM of a TFLIB cross section

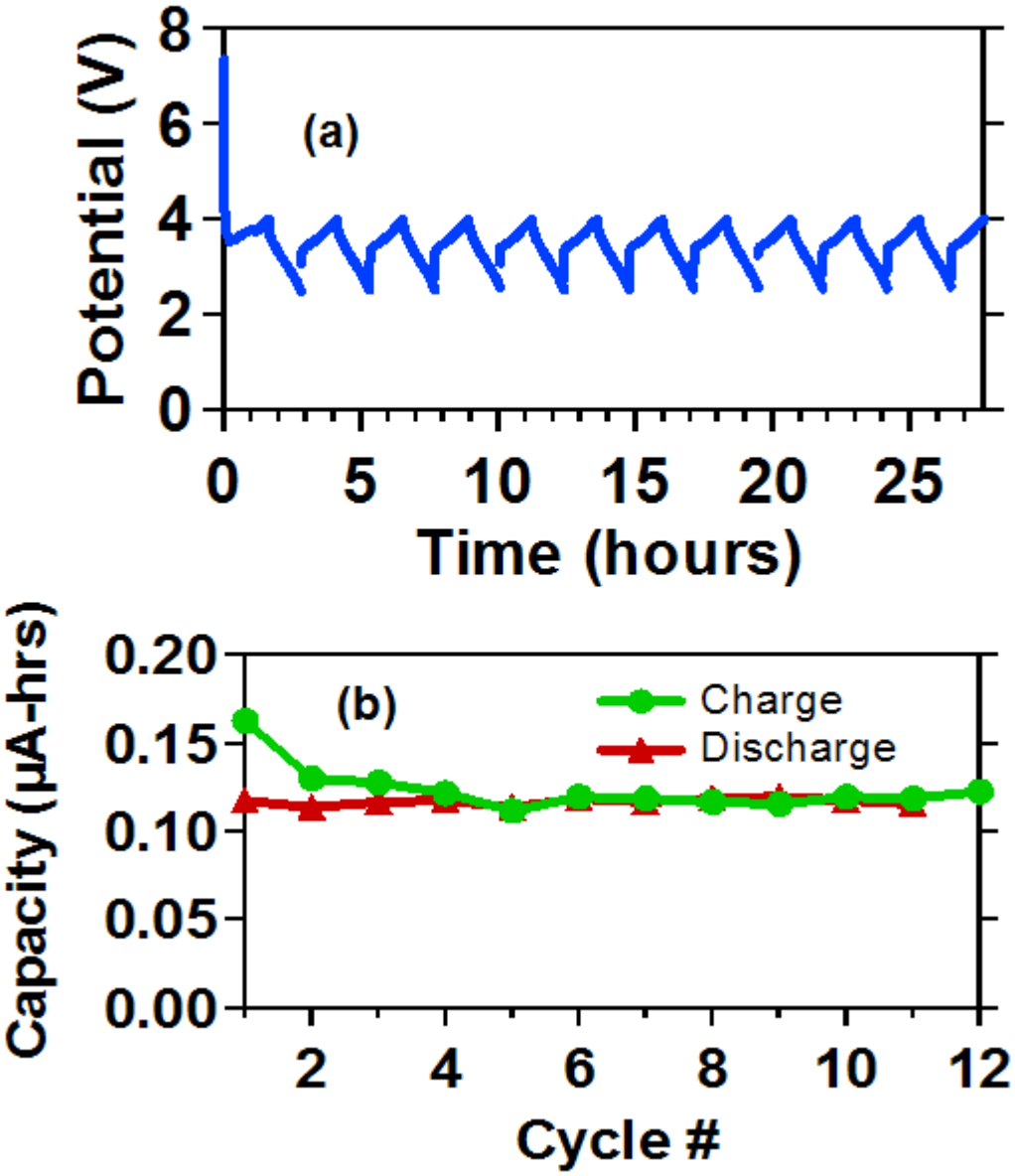

Figure S2 (a) Charge-discharge curves at 10^{-7} A and (b) calculated capacity for a thin film LIB with 0.007 cm^2 active area.

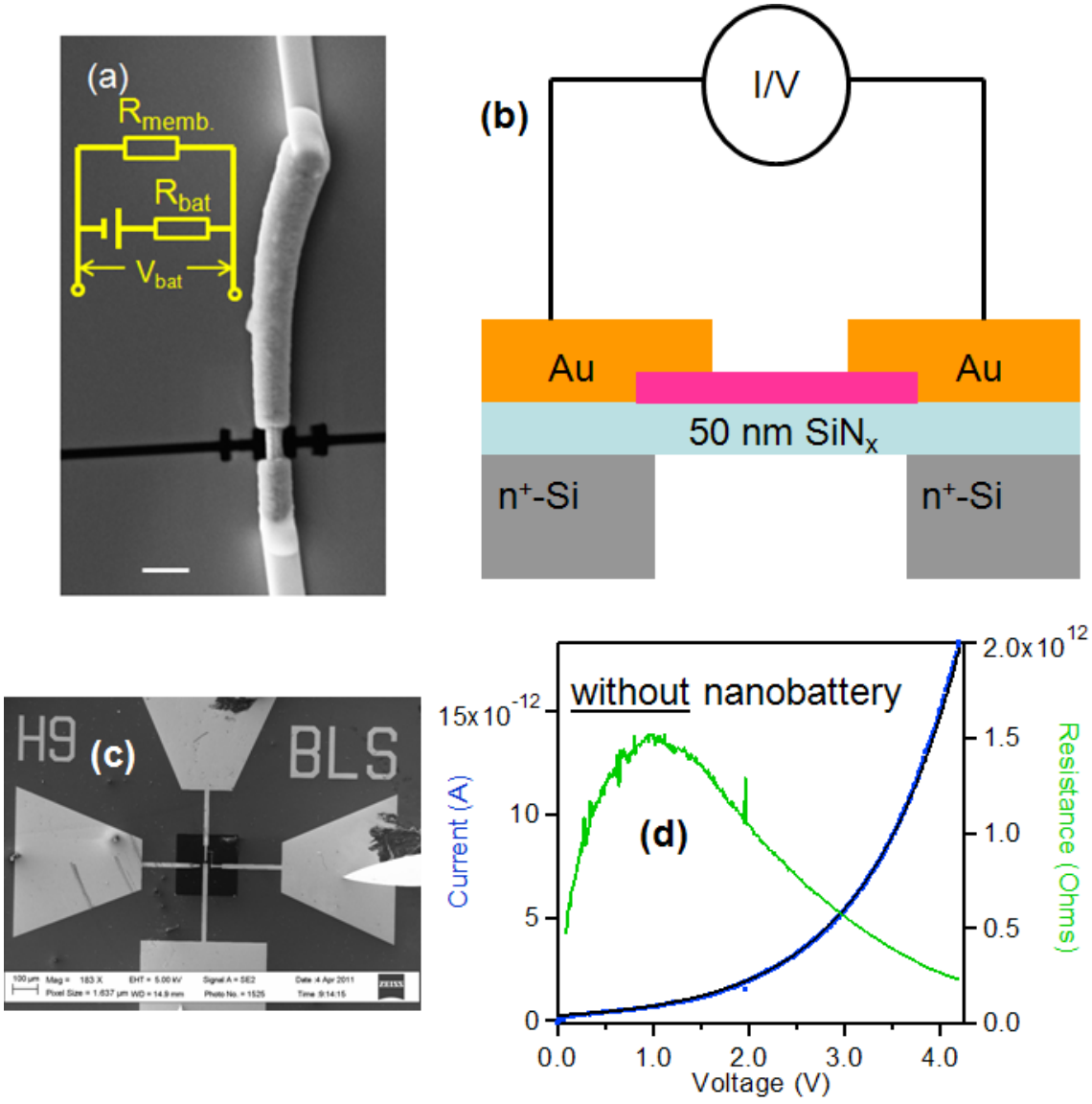

Figure S3 (a) FESEM image of a NWLIB on a SiN_x membrane with a schematic of the equivalent circuit, R_{memb} and R_{bat} are both voltage dependent; (b) schematic of the in situ biasing chip; (c) FESEM of the chip showing the Au contact pads; (d) I-V characteristics (blue) and effective resistance (green) for a Si chip without a nanowire.

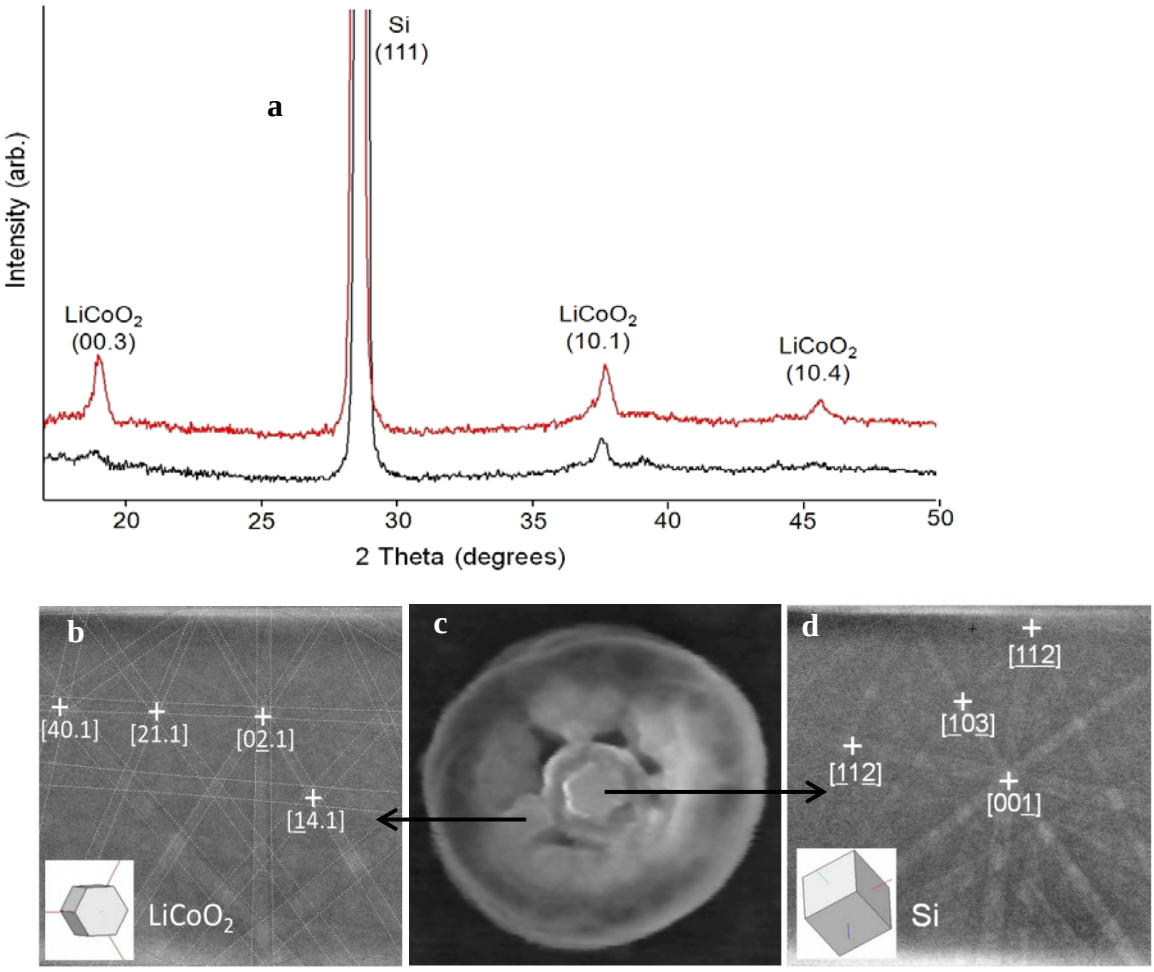

Figure S4. (a) XRD Ω-2Θ scans from the NW battery array. Phases detected: Si (substrate and NWLIBs, red curve) and $LiCoO_2$, while peaks from LiPON and thin Ti/Pt/Ti layers were not registered. $LiCoO_2$ indices correspond to the hexagonal phase (R-3m; PDF#75-0532) with lattice parameters *a*=2.817 Å and *c*=14.052 Å. Removal of NWs from substrate (black curve) has dramatically reduced (003) peak intensity, which implies that the observed texture in scan (a) is associated with $LiCoO_2$ shell on Si NWs. The $LiCoO_2$ texture in the shell was confirmed by EBSD analysis. EBSD patterns of the $LiCoO_2$ crystallites (b) and a Si nanowire (d), obtained from the cross-sectioned NWLIB (c) as indicated by arrows. Inset with simulated orientation of $LiCoO_2$ unit cell in (b) indicates that the (00.3) plane has preferred orientation nearly parallel to the Si (111) plane: the misorientation angle between [00.3] and [111] is 8°.

Model for space-charge limited conduction with traps

The general model for space-charge limited transport with traps describes electron transport via drift together with Poisson's equation for the electric field:

$$J = e\mu nE$$

$$\epsilon \frac{dE}{dx} = \rho(x) = -e(n - n_0) - e\sum_j \left(n_{tj} - n_{tj,0}\right)$$

Here n_0 is the equilibrium density, and the sum in the 2nd term is over trap states, labeled by j, and e is the magnitude of electron charge. $n_{tj,0}$ is the equilibrium density of the j^{th} trap state. We assume a continuous distribution of trap energies: $D(E) = \left(\frac{N_t}{k_b T_c}\right)\exp\left[\frac{(E - E_c)}{kT_c}\right]$. We further assume that the trap space charge density is much larger than the injected charge density, so that $\rho(x) \approx N_t\left[F(x), F_0\right]$. Here $F(x)$ is the quasi-Fermi level and F_0 is the equilibrium Fermi level. N_t is simply the occupied trap density at position x:

$$N_t\left[F(x), F_0\right] = \int_{F_0}^{F(x)} \left(\frac{N_t}{k_b T_c}\right)\exp\left[\frac{(E - E_c)}{kT_c}\right] dE .$$

As described in the text, important parameters in the solution are: $\ell = \frac{T_c}{T}$ and $\Gamma = \left(\frac{N_t}{n_0}\right)\left(\frac{n_0}{N_c}\right)^{1/\ell}$. Using the regional approximation method leads to 3 distinct regimes in the current-voltage relation (expressed in terms of $V_0 = \frac{en_0 L^2}{\epsilon}$):

1. For $V < V_0 \frac{\Gamma(\ell+1)^2}{\ell(2\ell+1)}$, $J = \frac{e^2 n_0^2 \mu L}{\epsilon}\frac{1}{2A}\left[1 - \sqrt{1 - \frac{4\epsilon AV}{en_0 L^2}}\right]$, where $A = \frac{\ell^2}{\Gamma(\ell+1)(2\ell+1)}$. The low voltage end of this regime corresponds to simple Ohmic Transport.

2. For $V_0 \frac{\Gamma(\ell+1)^2}{\ell(2\ell+1)} < V < \frac{4}{3} V_o \left(\frac{\Gamma(l+1)^2}{l(2l+1)} \right)^{l/l-1}$, there is not an explicit $J-V$ relation.

The solution is described through implicit relations involving the variables $v, w,$ and u. v and w are related to J and V according to:

$$J = \frac{e^2 n_0^2 \mu L}{\epsilon} \frac{1}{w}$$

$$V = \frac{e n_0 L^2}{\epsilon} \frac{v}{w^2}$$

The $J-V$ relationship is extracted via the parametric equations in u:

$$w = \frac{1}{2}\left[\frac{2\ell}{\Gamma(\ell+1)} \right]^{2\ell/(\ell-1)} + \frac{\ell}{\Gamma(\ell+1)} \left[u^{(\ell+1)/\ell} - \left(\frac{2\ell}{\Gamma(\ell+1)} \right)^{(\ell+1)/(\ell-1)} \right]$$

$$v = \frac{1}{3}\left[\frac{2\ell}{\Gamma(\ell+1)} \right]^{3\ell/(\ell-1)} + \frac{\ell}{\Gamma(2\ell+1)} \left[u^{(2\ell+1)/\ell} - \left(\frac{2\ell}{\Gamma(\ell+1)} \right)^{(2\ell+1)/(\ell-1)} \right]$$

At the onset of this regime, the current-voltage relation can be approximated by:

$$J \approx N_c \mu e^{(1-\ell)} \left[\frac{\epsilon \ell}{N_t (\ell+1)} \right]^{\ell} \left(\frac{2\ell+1}{\ell+1} \right)^{(\ell+1)} \frac{V^{(\ell+1)}}{d^{(2\ell+1)}}$$

3. For $V > \frac{4}{3} V_o \left(\frac{\Gamma(l+1)^2}{l(2l+1)} \right)^{l/l-1}$, we recover trap-free space charge limited transport:

$$J = \frac{9}{8} \epsilon \mu \frac{V^2}{d^3}.$$

For the current-voltage relation during the downward voltage sweep, we assume that all of the traps are occupied so that we may treat the problem as a trap-free insulator. We find that approximating the total current as the sum of thermal and SCLC current matches the exact solution well. The current-voltage relation is therefore simply:

$J = ne\mu \frac{V}{d} + \frac{9}{8} \epsilon \mu \frac{V^2}{d^3}$ over the entire voltage range.

We next comment on using a one-dimensional model for the cylindrical geometry of the nanowire battery. The inner wire radius r_1 is approximately 345 nm, while for the

thin layer the LiPON thickness d is 110 nm. The validity of the 1-d model can be checked by expanding the cylindrical solution in powers of $\frac{d}{r_1}$. For illustration, in the Ohmic regime the current-voltage relation is:

$$J\left(r_1\right) = e\mu n \frac{V}{r_1 \log\left[1+\frac{d}{r_1}\right]} \approx e\mu n \frac{V}{d}\left(1+\frac{1}{2}\left(\frac{d}{r_1}\right)+\ldots\right).$$

A similar (though more involved) analysis applies for the SCLC regime. We therefore estimate that values obtained with the one-dimensional model are within 30% of those obtained from the full cylindrical model, and is sufficient to capture the qualitative features of the electron transport.